Energy & Environmental Science

ROYAL SOCIETY OF CHEMISTRY

PAPER

View Article Online
View Journal | View Issue

Check for updates

Cite this: *Energy Environ. Sci.*, 2025, **18**, 5599

Charge carrier management for highly efficient perovskite/Si tandem solar cells with poly-Si based passivating contacts†

Xuzheng Liu, [ab] Michael Rienäcker, [cd] Mohammad Gholipoor, [ab] Lingyi Fang, [ab] Tonghan Zhao, [a] Benjamin Hacene, [b] Julian Petermann, [ab] Ruijun Cai, [b] Hang Hu, [ab] Thomas Feeney, [b] Faranak Sadegh, [ab] Paul Fassl, [ab] Renjun Guo, *[ab] Uli Lemmer, [ab] Robby Peibst *[cd] and Ulrich Wilhelm Paetzold *[ab]

Integrating wide-bandgap organic–inorganic lead halide perovskite absorber layers with Si bottom solar cells into tandem architectures offers significant potential for increasing power conversion efficiency (PCE). However, achieving high-performance monolithic tandem devices remains challenging, particularly when processing perovskite top cells on top of industrial silicon bottom cells, featuring polycrystalline silicon on oxide (POLO) passivating contacts, as implemented in "TOPCon" solar cells. Here, we employ an advanced silicon bottom cell architecture incorporating full-area electron-selective POLO front contacts and laser-structured hole-selective POLO back contacts. We perform the N_2 annealing at an elevated temperature of silicon bottom cells, effectively curing sputter-induced damage in the full-area electron-selective POLO contact of the recombination junction and enhancing the interface between transparent conductive oxide and the n-type doped poly-Si layer. Additionally, this annealing treatment likely improves the rear small-area contact between the aluminum (Al) and the p^+ poly-Si. Furthermore, we investigate how the nickel oxide layer regulates the substrate morphology and affects the charge carrier mechanisms for the top perovskite solar cells. These strategies remarkably promote charge carrier management, achieving a monolithic perovskite/POLO-Si tandem solar cell with a PCE of 31%. Moreover, the unencapsulated tandem cell retained 93% of its initial efficiency after operating for 240 hours at maximum power point under one sun intensity, 25 °C, and 30% relative humidity (ISOS-L-1), the extrapolated T_{80} lifetime is estimated to be 740 hours.

Received 14th March 2025,
Accepted 28th April 2025

DOI: 10.1039/d5ee01486g

rsc.li/ees

Open Access Article. Published on 06 May 2025. Downloaded on 1/30/2026 3:27:15 AM.
This article is licensed under a Creative Commons Attribution 3.0 Unported Licence.

Broader context

Integrating perovskite as the top absorber with a silicon bottom cell to form a tandem device is a key approach to surpassing the Shockley–Queisser (SQ) limit. However, research on the recombination junction for silicon featuring polycrystalline silicon on oxide (POLO) passivating contacts remains relatively scarce, and the high-quality perovskite growth on POLO-Si presents crucial challenges. Here, we demonstrate an annealing treatment at elevated temperatures to improve the recombination junction, likely improve the rear point contacts as well, and investigate the impact of hole transport layers (HTLs) on charge carrier dynamics in the perovskite layer from material selection and morphology regulation. These strategies effectively enhance charge carrier management in the tandem solar cells. Finally, we achieve a PCE of 31% in a perovskite/POLO-Si tandem solar cell. Our findings illustrate how charge carrier management improvements in the tandem devices enable the integration of perovskite top cells onto POLO-Si bottom solar cells, paving the way for further progress in perovskite/silicon tandem solar cells based on POLO-Si.

[a] *Institute of Microstructure Technology (IMT), Karlsruhe Institute of Technology (KIT), Hermann-von-Helmholtz-Platz 1, Eggenstein-Leopoldshafen, 76344, Karlsruhe, Germany. E-mail: renjun.guo@kit.edu, ulrich.paetzold@kit.edu*
[b] *Light Technology Institute (LTI), Karlsruhe Institute of Technology (KIT), Engesserstrasse 13, 76131, Karlsruhe, Germany*
[c] *Institute for Electronic Materials and Devices, Leibniz University Hannover, Schneiderberg 32, 30167, Hannover, Germany. E-mail: peibst@isfh.de*
[d] *Institute for Solar Energy Research Hamelin (ISFH), Am Ohrberg 1, 31860, Emmerthal, Germany*

† Electronic supplementary information (ESI) available. See DOI: https://doi.org/10.1039/d5ee01486g

Open Access Article. Published on 06 May 2025. Downloaded on 1/30/2026 3:27:15 AM.
This article is licensed under a Creative Commons Attribution 3.0 Unported Licence.

The field of high-efficiency solar cells has witnessed rapid advancements in the power conversion efficiency (PCE) of monolithic perovskite–silicon tandem solar cells (PSTSCs), with the current record reaching 34.6%. This significantly exceeds the highest reported efficiencies for single-junction perovskite solar cells (PSCs) and silicon solar cells which are 27.0% and 27.4%,[1] respectively. Although cell sizes and technology maturity are not comparable yet, these record efficiencies indicate that combining metal halide perovskites with silicon solar cells to form PSTSCs surpasses the 33.7% Shockley–Queisser limit for single-junction solar cells.[2] Among these tandem configurations, two-terminal perovskite–silicon tandem solar cells (2T-PSTSCs), which directly connect a crystalline silicon (c-Si) bottom solar cell with a perovskite top cell, have emerged as the most promising candidates. Currently, mainstream tandem solar cell research focuses on heterojunction Si (SHJ-Si), while research progress on tandem cells based on alternative Si-PV technologies, particularly those utilizing poly-Si-based passivating contacts, has been comparatively slower.[3–14] These contacts are widely known as ''tunnel oxide passivated contacts'' (TOPCon) but can more generally be referred to as polycrystalline silicon on oxide (POLO) passivating contacts.[15] Several challenges hinder the integration of POLO-Si in tandem configurations: (1) the decent passivation quality of the poly-Si passivating contacts on textured surfaces, hindering the application of a double-sided texturing process and resulting in weaker light management and limited short-circuit current density (J_{SC}),[16–19] (2) insufficient studies on recombination junctions for poly-Si passivating contacts,[20] and (3) a limited understanding of perovskite growth mechanisms on poly-Si passivating contact surfaces.[16–19,21,22]

However, poly-Si-based passivating contacts-Si technology still offers significant advantages. First, industrial Si cell featuring POLO contacts have demonstrated the potential for high efficiency on large area, reaching up to 26.58%.[23] Second, Si cells with POLO contacts has more significant cost-reduction potential compared to SHJ-Si, as its ultrathin silicon oxide (SiO_x) and doped polycrystalline silicon (poly-Si) layers are more cost-effective than the high-quality amorphous silicon (a-Si: H) layers used in SHJ-Si.[24–26] Moreover, the Si solar cell with POLO contacts is compatible with existing PERC (Passivated Emitter and Rear Cell) fabrication lines, allowing for easier industrial integration.[27] Finally, POLO-Si technology reduces the consumption of critical materials such as silver and indium compared to SHJ-Si, enhancing the sustainability of large-scale production.[28] Given these advantages, we focus on tandem solar cells (TSCs) based on Si cells with POLO contacts.

Here, we employ a Si bottom cell featuring POLO contacts (POLO-Si bottom cell) with an optimized charge carrier management strategy. The Si bottom solar cell features poly-Si passivating contacts for electrons and holes, implemented on a 275 μm thick n-type float zone wafer. The front side is chemically mechanically polished (CMP) for an electron-collecting passivating n-type doped poly-Si on oxide junction, while the rear side employs partially textured hole-collecting poly-Si passivating contact covering 25% of the total area,[29] while the remaining area is alkaline textured. This ''point emitter'' design balances optical and electrical properties. Since p-type doped poly-Si on oxide junctions only exhibit a decent passivation quality on textured surfaces, we restrict these junctions to planar regions covering only 25% of the total area.[30] The triple-cation perovskite $Cs_{0.05}(FA_{0.77}MA_{0.23})_{0.95}Pb(I_{0.77}Br_{0.23})_3$ (1.68 eV) are utilized as the top absorber layer, following the processing established in our previous work.[31] We propose that annealing at elevated temperatures under a nitrogen atmosphere effectively improves the recombination junction regarding curing sputter-induced damage and reducing contact resistance. While the annealing process likely enhances the TCO/n^+ poly-Si interface, its impact on the rear Al/p^+ poly-Si contact may further decrease the overall series resistance. Such treatment enhances the charge carrier transport and allows for efficient operation as a sub-cell in the tandem architecture. Furthermore, we develop an ultrathin sputtered 5 nm nickel oxide (NiO_x) combined with a self-assembled monolayer (SAM) as the HTL. The NiO_x layer forms a discontinuous micro-island morphology that substantially increases the specific surface area (SSA), improving SAM adhesion and providing nucleation sites for the perovskite growth. The SAM passivates interfacial defects, suppressing non-radiative recombination and improving charge carrier management. As a result, we successfully integrate the perovskite top solar cell with the POLO-Si bottom solar cell into a highly efficient tandem solar cell with a PCE of 31%, and the unencapsulated tandem cell retains 93% of its initial efficiency after operating for 240 hours at maximum power point under 1 sun, 25 °C, and 30% relative humidity (ISOS-L-1). The extrapolated T_{80} lifetime is estimated to be 740 hours.

Results and discussion

An innovative silicon bottom cell architecture schematically shown in Fig. 1(A) is developed, incorporating advanced POLO junctions and alkaline surface texturing. This configuration enhances charge carrier selectivity and light management, effectively reducing recombination losses and increasing photocurrent generation. The improvements in electrical and optical performance provide a solid foundation for high-efficiency perovskite/silicon tandem cells.

The front side of the bottom solar cell, full-area passivated by an electron-collecting n^+ POLO junction, is intentionally maintained planar. This design matches the rear surface morphology of today's industrial ''TOPCon'' Si solar cells, where the same junction is typically applied but flipped upwards for tandem integration. Planar n^+ POLO junctions facilitate J_0 values down to 0.5 fA cm^{-2}, comparable to the best alternative electron selective contacts, such as H-rich amorphous-Si/crystalline Si heterojunctions.[32] Nevertheless, it would also be possible to apply these n^+ POLO junctions on an alkaline textured surface with random pyramids, while this modification results in a slight increase in the recombination current density to ~2 fA cm^{-2}. In contrast, the hole-collecting p^+ POLO contact shows relatively low recombination losses with J_0 value of 1.8 fA cm^{-2} on planar surfaces.[32] However, when applied to

 This journal is © The Royal Society of Chemistry 2025

Open Access Article. Published on 06 May 2025. Downloaded on 1/30/2026 3:27:15 AM.
This article is licensed under a Creative Commons Attribution 3.0 Unported Licence.

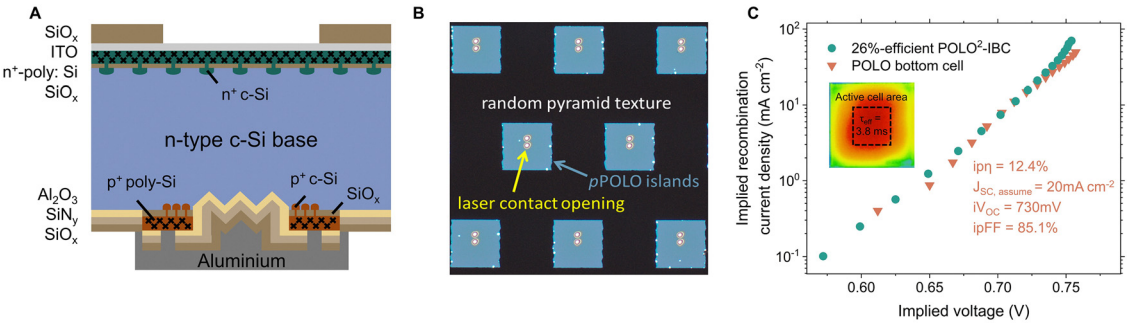

Fig. 1 (A) Schematic illustration of a silicon bottom solar cell with a polished front side and a partially textured rear side. The solar cell features locally passivated p^+ POLO contacts on the rear side and a full area n^+ POLO contact on the front side. (B) Optical micrograph of the rear side of the silicon bottom cell in (A) before aluminum deposition, highlighting the locally passivated p^+ POLO contact regions. (C) Implied recombination current density as a function of implied voltage for 26%-efficient POLO^2-IBC single junction cell and the POLO bottom cell. Parameters can be derived from injection-dependent lifetime characteristics based on the infrared lifetime mapping method.

textured surfaces, p^+ POLO contact on textured surfaces suffers from fundamentally higher recombination rates,[29] exceeding 20 fA cm^{-2}. Thus, if implemented across the entire rear side of the bottom cell, this elevated recombination would lead to a substantial drop in open-circuit voltage (V_{OC}) by about 20–30 mV. On the other hand, a planar rear side would, in combination with the also planar front, only yield poor light trapping.[33] To balance electrical and optical properties, a partially textured rear side is adopted, optimizing both carrier extraction and photon management in the tandem architecture.

To optimize the trade-off between carrier extraction and optical performance, we apply the hole-collecting p^+ POLO contacts on localized planar "island-shaped" regions while texturing most of the rear surface (~75%). The textured areas are effectively passivated by a dielectric $Al_2O_3/SiN_x/SiO_x$ stack, which also serves as a rear reflector, as shown in Fig. 1(B). The structuring process is implemented *via* a laser ablation technique adapted for precise patterning.[34,35] From a laser alignment precision perspective, the 25% area fraction of p^+ POLO contacts could be further reduced below 5% to enhance light trapping. However, this must be balanced against the local nature of minority carrier collection, particularly for holes in our n-type doped silicon wafer. Traditionally, Si-PV have assumed that the minority carrier-collecting contact must be as large as possible to minimize recombination-induced extraction losses.[30] However, for devices on defect-free wafers and with efficient surface passivation, such as on our bottom cells, as well as state-of-the-art interdigitated back-contact (IBC) solar cells,[36] such a conventional assumption no longer holds. In these advanced architectures, minority carriers can diffuse laterally to be collected at localized contacts with minimal recombination losses. In this work, we present the excellent minority carrier collection by only 25% area coverage of the hole-collecting p^+ POLO contact by high external quantum efficiency (EQE) values close to 100% for the bottom cell. We, therefore, conclude that further reducing the p^+ POLO area fraction would still be compatible with efficient minority carrier collection. Another aspect inherent to local minority carrier extraction is entropy-induced "resistive losses" for the diffusion of minority carriers.[37,38] Such losses are only significant for high wafer doping, which means reduced minority carrier concentration and thus increased entropy-induced "resistive loss" for minority carriers. However, they remain minor for our lightly doped 3.3 Ω cm base material.

We validate the exceptional electronic performance of our POLO-Si bottom cells by the injection-dependent infrared lifetime mapping.[39] The suns-implied open circuit voltage curve is shown in Fig. 1(C). The corresponding curve for our 26.1% efficient POLO Si single junction IBC cell[40] – NREL efficiency chart record for non-heterojunction Si solar cells from 2018 up to now is also shown.[41] Notably, from the 600–725 mV voltage range, the two curves overlap, demonstrating high implied open-circuit voltages and a steep slope of ~60 mV per decade, corresponding to an ideality factor of one. This absence of deviation indicates negligible Shockley–Read–Hall (SRH) recombination in lightly doped or carrier-depleted regions, such as space charge regions, and no observable balancing currents between well-passivated and recombination-active areas. If either of these effects were present, the ideality factor would increase, reducing the slope of the suns-implied open circuit voltages (iV_{OC}) curve. This is remarkable since laser cutting diced the solar cells from a larger wafer to one-inch substrates. Indeed, the inset in Fig. 1(C) shows increased recombination near the laser-cut edges, but it does not affect the active cell area as indicated by the dashed square. For $iV_{OC} > 730$ mV, the slope of the suns-implied open circuit voltage curves for the POLO bottom cell remains constant, whereas it increases for the IBC solar cell. This divergence can be attributed to a transition in the silicon substrate from low-level to high-level injection, altering the ideality factor of dominant Auger recombination from 1 to 2/3. The fact that the POLO bottom solar cell does not show this transition is tentatively attributed to slightly higher surface recombination of ~10 fA cm^{-2} compared to ~6 fA cm^{-2} in the IBC solar cell. Therefore, Auger recombination dominates in the IBC cell at a lower iV_{OC} threshold than in the POLO bottom solar cell.

When assuming a photogeneration current density of 20 mA cm^{-2} in the Si bottom solar cell when filtered by the perovskite top solar cell, we estimate an iV_{OC} of 730 mV, an implied pseudo fill factor (ipFF) of 85.1%, resulting in an implied pseudo efficiency (iPCE) of 12.4%. One should note

Open Access Article. Published on 06 May 2025. Downloaded on 1/30/2026 3:27:15 AM.
This article is licensed under a Creative Commons Attribution 3.0 Unported Licence.

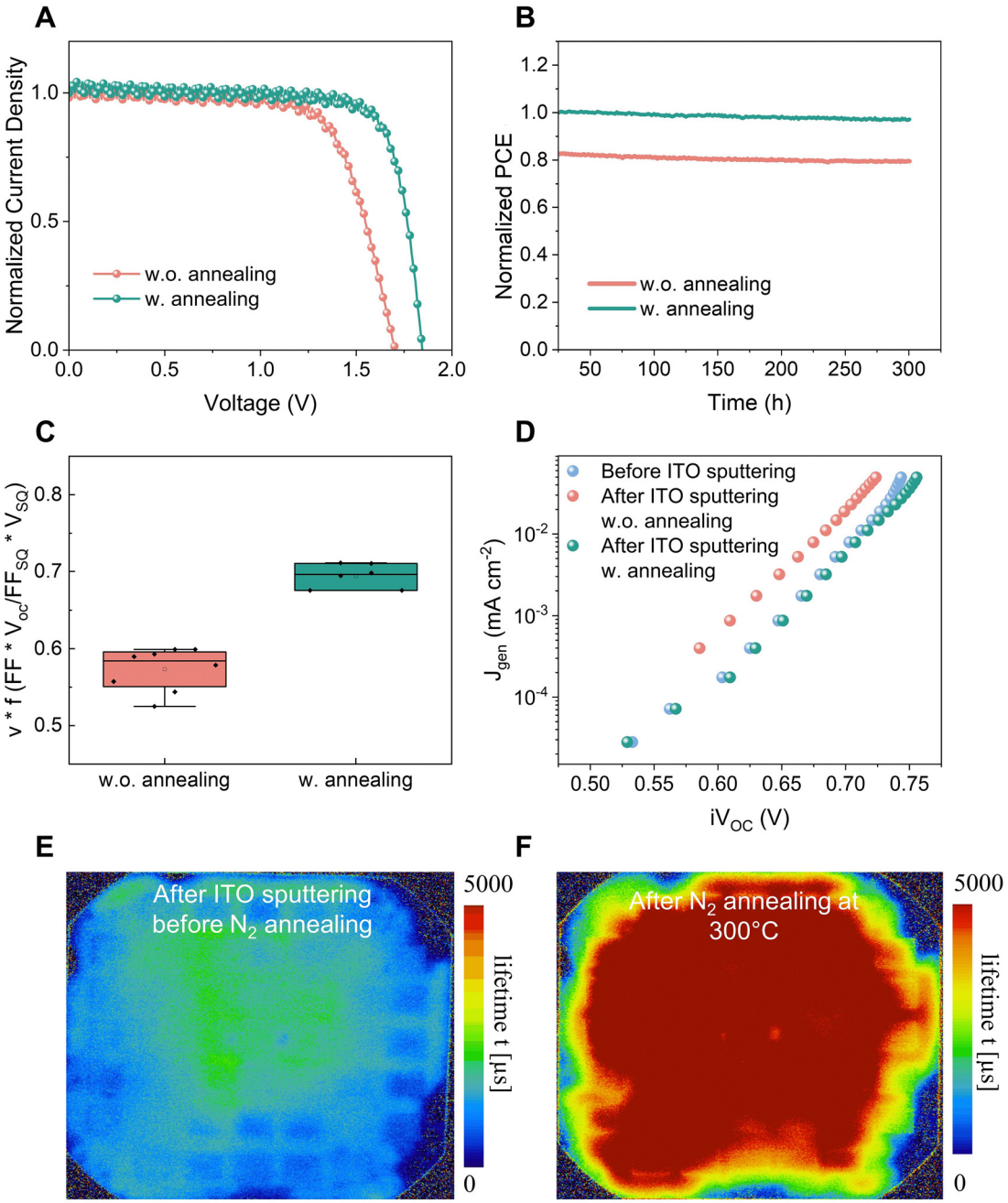

Fig. 2 (A) Current density–voltage (J–V) characteristics comparing tandem devices without and with N_2 annealing at 300 °C. The annealed device exhibits improved FF and V_{OC}, indicating enhanced charge transport and reduced recombination losses. The normalized J highlights the effect of annealing on V_{OC} and FF. (B) The MPPT measurements of normalized PCE over 5 min, which confirm that the annealing treatment does not harm the operational stability of tandem devices. (C) Distribution of $v \times f$ of the tandem solar cells (16 devices in total) without and with annealing treatment. Here, $v \times f$ can be derived from $v \times f = FF \times V_{OC}/FF_{SQ} \times V_{SQ}$, which refers to voltage and fill factor fraction for tandem cells. The increase suggests reduced resistive losses and enhanced passivation towards better charge carrier management. (D) The pseudo-JV curves of POLO-Si bottom cell before ITO sputtering and after ITO sputtering w.o. and w. annealing. The discrepancy between the pseudo-JVs and the real JVs reveals an additional effect of annealing. Beyond improving the TCO/n^+ poly-Si interface on the front side, annealing might influence the Al/p^+ poly-Si contact on the rear side as well, further lowering the overall contact resistance and improving the interface, thus leading to overall enhanced charge carrier management and a pronounced improvement in FF and V_{OC}. (E) and (F) Infrared lifetime mapping of the Si bottom solar cell before and after annealing. (E) Before annealing, the map exhibits non-uniform carrier lifetime distribution with lower values, suggesting defects or damage induced by ITO sputtering. (F) After annealing, a significant increase in carrier lifetime is observed, with a more homogeneous distribution across the entire cell, indicating effective defect healing and improved passivation.

that in the final J–V measurement of the tandem device, minor series resistance-induced losses are expected. More severe, the abovementioned measurements are performed under total area illumination. When performing an aperture area measurement with shadow masks, both V_{OC} and fill factor (FF) are expected to reduce due to recombination-active parallel diodes in the dark.[42]

This journal is © The Royal Society of Chemistry 2025

Open Access Article. Published on 06 May 2025. Downloaded on 1/30/2026 3:27:15 AM. This article is licensed under a Creative Commons Attribution 3.0 Unported Licence.

The recombination junction is a pivotal component in TSCs, functioning as a bridge between the two sub-cells and ensuring their successful integration. However, when fabricating 1.68 eV wide-bandgap PSCs on the POLO-Si bottom cell, the initial tandem device performance is suboptimal. A key limiting factor is damage to the POLO junctions during the sputtering process of the indium tin oxide (ITO) layer, which degrades passivation quality—an issue previously reported in similar studies.[43–45] This damage decreases the carrier-selectivity of the n^+ POLO junction, resulting in increased SRH recombination at the c-Si wafer/SiO_x interface, reducing V_{OC} and a lower ipFF, ultimately limiting the final FF in the tandem cells. Moreover, the rear point contact at aluminum (Al)/p^+ poly-Si layer may exhibit relatively high contact resistance, hindering V_{OC} and FF.

To overcome the integration challenge, we apply an annealing treatment of the ITO-coated silicon bottom cell at elevated temperatures (300 °C) in a nitrogen atmosphere. This process significantly improves the performance of tandem devices compared to those without annealing. Fig. 2(A) presents the tandem solar cell current density–voltage (*J*–*V*) characteristics without and with annealing treatment. The normalized current density highlights the crucial impact of annealing treatment on enhancing charge carrier transport and extraction, specifically by improving V_{OC} and FF of tandem devices. The unannealed device exhibits lower FF and V_{OC}. The perovskite films grown on unannealed and annealed silicon bottom solar cells exhibit similar PLQY and iV_{OC} (see Fig. S4, ESI†), suggesting that the performance enhancement of the tandem device due to annealing primarily originates from its effect on the silicon bottom solar cell. The first aspect is induced by a reduction of the recombination-limited pseudo-fill factor and an increased series resistance. The high series resistance might be due to some remaining native oxide between the ITO and the n^+-poly-Si. Additionally, the sputtering process degrades the POLO contact quality beneath the ITO layer, leading to defects at the n^+ poly-Si/ITO interface which increase non-radiative recombination and further reduce V_{OC}.

The N_2 annealing of the Si bottom solar cell before depositing the HTL of the perovskite top solar cell improves both V_{OC} and FF, resulting in better PCE. The MPPT results in Fig. 2(B) demonstrates that the annealing treatment does not suppress the operational stability of the tandem device. The results in Fig. 2(A) and (B) show that the sputtering process used for depositing the recombination junction induces pronounced V_{OC} loss and carrier transport loss in tandem devices, the annealing significantly cures the sputtering-induced damage. Fig. 2(C) presents the statistical distribution of $v \times f = FF \times V_{OC}/FF_{SQ} \times V_{SQ}$ for a batch of unannealed and annealed tandem devices (16 devices in total), we apply $v \times f$, defined as the voltage and fill factor fraction ($v \times f = FF \times V_{OC}/FF_{SQ} \times V_{SQ}$) for tandem solar cells, to describe the total electrical limitations of the device and to quantify charge carrier management, including the recombination of charge carriers in the bulk, surfaces, and interfaces.[46] It is evident that the $v \times f$ of the annealed devices is overall higher than that of the unannealed devices, increasing from 0.58 to 0.7, with a narrower performance distribution. This indicates that annealing treatment effectively improves charge carrier management.

The pseudo-*JV*s in Fig. 2(D) curves are constructed for Si solar cells with POLO contacts before ITO sputtering, after ITO sputtering without and with annealing (Parameters in Table S1, ESI†). Compared to the Si solar cell before ITO (iV_{OC} = 0.728 V, ipFF = 0.85), the Si bottom solar cell after ITO exhibits a lower iV_{OC} (0.7 V) and ipFF (0.83). While the device shows higher iV_{OC} (0.735 V) and ipFF (0.848) after N_2 annealing. This indicates that annealing enhances charge carrier management through curing sputter-induced damage to the recombination junction. Nevertheless, the iV_{OC} and ipFF difference of Si cells without and with annealing obtained from the pseudo-*JV*s do not fully align with the differences found in the real *J*–*V* curves. Given that pseudo-*JV* characterization is designed to minimize resistive loss and does not fully capture series resistance (R_S) effects such as from metal–semiconductor interfaces,[47,48] we speculate that another key source of high series resistance is likely the Al/p^+ poly-Si contact on the rear side, which occupies only 0.25% of the area.[49] This small contact fraction renders the device highly sensitive to minimal contact resistances of even 1 mΩ cm^2, leading to significant series resistance. Potentially residual SiO_x or Al_2O_3 remaining at the poly-Si surface after laser contact opening contributes to increased contact resistance. While hydrofluoric acid (HF) treatment mitigates this issue, high resistance due to insufficient treatment has been observed. Annealing at 300 °C may facilitate reactions between Al and the residual dielectric layer, effectively reducing the contact resistance, thereby lowering the overall series resistance and non-radiative recombination, and enhancing the V_{OC} and FF.

To verify the underlying mechanism, we employ the infrared lifetime mapping technique to characterize the effect of the N_2 annealing on the minority carrier lifetime in the silicon bottom cell. Fig. 2(E) and (F) present the spatially resolved charge carrier lifetime images of Si wafers before and after thermal annealing, followed by the sputtered ITO layer.[39,50] The minority carrier lifetime of the annealed silicon wafer shows a fourfold improvement compared to the unannealed wafer, with overall improved uniformity. The degradation is attributed to ion bombardment during sputtering, which damages the poly-Si layer by forming deep defects and Si dangling bonds.[44] Thermal annealing effectively repairs broken Si–Si bonds and recovers minority carrier lifetime notably. To validate this phenomenon at the device level, we perform numerical simulations (see Fig. S5 and parameters shown in Table S2, ESI†) to illustrate the impact of minority carrier lifetime on the performance of silicon solar cells, quantitatively elucidating the relationship between lifetime enhancement and improved device characteristics, demonstrating that sputtering-induced degradation at the recombination junction and rear contact severely suppresses minority carrier transport and reduces V_{OC}. Moreover, XRD and electrical analysis results reveal that the characteristic FWHM of the ITO (222) phase plane at 30.3° becomes smaller after annealing, indicating the enhanced crystallinity of on the (222) plane, and the square resistance

Open Access Article. Published on 06 May 2025. Downloaded on 1/30/2026 3:27:15 AM.
This article is licensed under a Creative Commons Attribution 3.0 Unported Licence.

of ITO layer decreases from 114.8 Ω □$^{-1}$ before annealing to 91.3 Ω □$^{-1}$ after annealing, suggesting the improved charge transfer property (see Fig. S6 and Table S3, ESI†).[51,52] Taken together, thermal annealing effectively repairs sputter-induced damage, improves the quality of ITO layer, and might improve the rear contacts, significantly reducing transport loss of charge carriers and the non-radiative recombination.

In addition to the annealing treatment for mitigating damage of the bottom cell after recombination layer deposition, the hole transport layers (HTLs) play a crucial role in TSCs. As the buried interface beneath the perovskite absorber, an optimized HTL facilitates efficient carrier extraction and regulates the crystallization and growth of the perovskite absorber layer. This results in a low-defect buried interface and a high-quality perovskite film, both essential for achieving high-efficiency TSCs.[53,54] Through a detailed study on morphology control and material selection of the HTL on the recombination junction of POLO-Si, an optimal HTL combination is ultimately identified, enabling excellent charge carrier management at the bottom side of the perovskite layer. To optimize the HTLs, we first investigate NiO_x layers of different thicknesses (5, 15, and 25 nm) and characterize their PLQY and time-resolved photoluminescence (TRPL) spectra. The PLQY results in Fig. 3(A) show that the sample with a 5 nm NiO_x layer exhibits higher PLQY and lower V_{OC} loss, indicating reduced non-radiative recombination. Additionally, the TRPL results (see Fig. S7, ESI†) reveal that the 5 nm NiO_x layer leads to a longer carrier lifetime, further supporting the enhanced passivation quality and suppressed non-radiative recombination processes.

To further suppress non-radiative recombination at the buried interface, we compare PLQY and TRPL for three cases: SAM-only, NiO_x-only, and NiO_x combined with SAM. The results

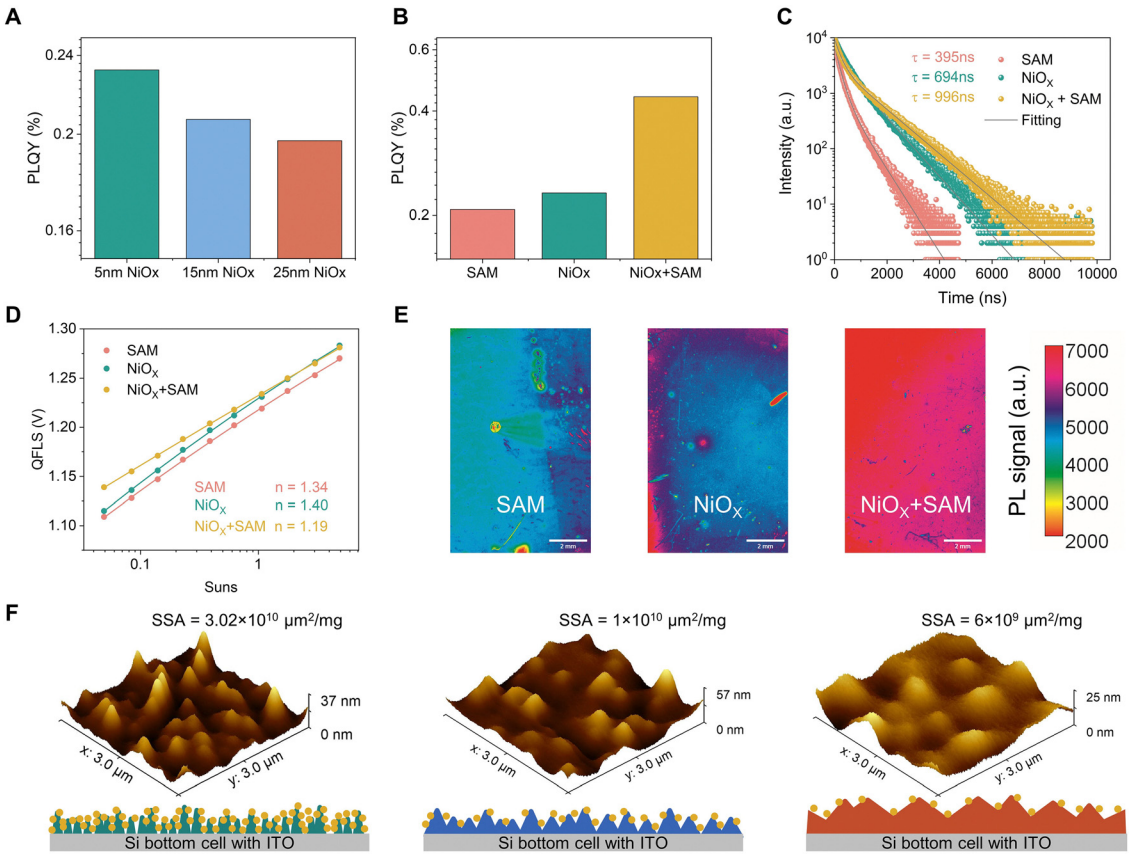

Fig. 3 (A) PLQY measurements performed on half stack samples (Si/ITO/NiO_x/2PACz/Perovskite) with different thicknesses of NiO_x (5, 15 and 25 nm), showing the highest PLQY at 5 nm, indicating better passivation and reduced non-radiative recombination. (B) PLQY across different HTL configurations (SAM-only, NiO_x-only, and NiO_x + SAM), demonstrating that the NiO_x + SAM combination yields the highest PLQY, suggesting improved interfacial charge carrier management. (C) TRPL measurements reveal prolonged carrier lifetimes for the NiO_x + SAM configuration (τ = 996 ns) compared to NiO_x alone (τ = 694 ns) and SAM-only (τ = 395 ns), confirming reduced non-radiative recombination and enhanced charge carrier extraction. (D) The Quasi-Fermi Level Splitting (QFLS) measurements show that the NiO_x + SAM configuration achieves the lowest ideality factor (n = 1.19), indicative of improved charge transport and suppressed recombination compared to NiO_x-only (n = 1.40) and SAM-only (n = 1.34). (E) PL intensity maps performed on half stack samples with different HTLs: Si/ITO/2PACz/Perovskite, Si/ITO/NiO_x/Perovskite, Si/ITO/NiO_x/2PACz/Perovskite, demonstrating improved film homogeneity. White scale bar: 2 mm. (F) 3D atomic force microscopy (AFM) images of Si bottom solar cells with NiO_x layer of different thicknesses (5, 15, 25 nm) and corresponding schematic diagrams of the morphology. The yellow dots indicate SAM molecules anchored onto the NiO_x layer. Surface morphology analysis shows that NiO_x + SAM forms a discontinuous micro-island structure on the recombination junction, increasing the specific surface area (SSA) significantly (3.02×10^{10} μm^2 mg^{-1}) compared to NiO_x-only (1×10^{10} μm^2 mg^{-1}) and SAM-only (6×10^9 μm^2 mg^{-1}). This enhanced SSA promotes better adhesion of SAM molecules, which could improve perovskite nucleation and growth.

 This journal is © The Royal Society of Chemistry 2025

Open Access Article. Published on 06 May 2025. Downloaded on 1/30/2026 3:27:15 AM. This article is licensed under a Creative Commons Attribution 3.0 Unported Licence.

in Fig. 3(B) and (C) indicate that the perovskite film on the NiO_x + SAM HTL exhibits the highest PLQY and the longest carrier lifetime (996 ns) among the three HTLs. Additionally, we conduct light-intensity-dependent PLQY measurements to extract the ideality factor and pseudo-*JV* characteristics of the perovskite layer based on these three HTLs. Fig. 3(D) shows a lower ideality factor (NiO_x + SAM = 1.19, SAM = 1.34, NiO_x = 1.40), indicating that 5 nm NiO_x effectively suppresses recombination pathways with high ideality factors such as SRH in high-level injection with SAM. The pseudo-*JV* curves (see Fig. S8 and Table S4, ESI†) reveal that the NiO_x + SAM sample achieves the highest in both iV_{OC} and pseudo-FF (iV_{OC} = 1.233 and pFF = 86.6), reinforcing its role in enhancing carrier extraction and minimizing recombination losses. These improvements can be attributed to the ability of NiO_x + SAM to regulate the crystallization and growth of the perovskite absorber, thereby improving the material uniformity and reducing defect densities at the interface. This conclusion is further supported by PL intensity mapping as shown in Fig. 3(E), where the NiO_x + SAM sample exhibits the highest and most uniform PL intensity. In contrast, the SAM-only sample shows lower PL intensity and poorer uniformity, while the NiO_x-only sample exhibits weaker PL intensity, confirming inferior passivation and higher non-radiative recombination.

Finally, to understand why the combination of SAM with a 5 nm NiO_x layer achieves optimal charge carrier management, we employ atomic force microscopy (AFM) to investigate the surface morphology of NiO_x layers with different thicknesses (5, 15, 25 nm) grown on POLO-Si. The surface of the silicon cells without ITO and NiO_x layers exhibits isolated islands (see Fig. S9A, ESI†), which can be attributed to the morphology of the poly-Si layer, since the poly-Si layer thickness is reduced from 220 nm to 110 nm by oxidation and further to approximately 30 nm by isotropic etching. The oxidation process is found to proceed faster at grain boundaries, leading to a certain degree of surface roughness.[55] The ITO layer, serving as a recombination junction, tends to grow preferentially along the grain boundaries of the poly-Si layer during sputtering, gradually forming a continuous film with some surface roughness once a certain thickness is reached, which originates from the roughness of the underlying poly-Si layer (see Fig. S9, ESI†). In Fig. 3(F), upon sputtering a 5 nm NiO_x layer, the NiO_x grows around the pre-existing islands, forming medium-sized islands and generating small islands on the planar surface (This morphology can be further supported by the SEM and EDX results in Fig. S10, ESI†). Increasing the NiO_x thickness to 15 nm leads to further growth and coalescence of the small and medium-sized islands, gradually forming a continuous thin film. At 25 nm thickness, the islands fully merge, forming a dense, interconnected film with a reduced specific surface area. The densely distributed small-size island morphology of the 5 nm NiO_x significantly increases the specific surface area of 3.02×10^{10} μm^2 mg^{-1} compared to the 15 nm (1×10^{10} μm^2 mg^{-1}) and 25 nm NiO_x layers (6×10^9 μm^2 mg^{-1}). This unique interfacial structure likely plays a crucial role in reducing non-radiative recombination losses and improving charge carrier management by ensuring better molecular self-assembly and charge transport at the buried interface. We hypothesize that this mechanism effectively minimizes non-radiative losses, and improves charge carrier management.

Notably, for small-area perovskite single-junction solar cells fabricated in our lab, SAM alone performs best as the HTL (see Fig. S11, ESI†). This highlights the differences between single-junction and tandem devices, which is essential to systematically analyze and understand the perovskite layer grown on a silicon bottom solar cell rather than directly extrapolating conclusions from single-junction solar cells to tandem devices.

Based on the annealing treatment of POLO-Si bottom solar cell and optimization on the HTL side (specifically the sputtered NiO_x and SAM), we develop a reliable recombination junction integrating the perovskite top cell with the high-performance Si bottom solar cell with POLO contacts. The schematic illustration of the 2T-PSTSC is shown in Fig. 4(A). The ITO layer serves as the recombination layer, electrically interconnecting the perovskite top cell and the silicon bottom cell. In the perovskite top cell, a well-investigated triple-cation perovskite composition (1.68 eV) of $Cs_{0.05}(FA_{0.77}MA_{0.23})_{0.95}Pb(I_{0.77}Br_{0.23})_3$ is employed as the absorber layer. The top cell architecture consists of ITO/NiO_x + 2PACz/Perovskite/$PDAI_2$ + BAI/C_{60}/SnO_x/IZO/Ag/MgF_2. The cross-sectional SEM image of the PSTSC shows (see Fig. S12, ESI†) that the perovskite layer has a thickness of approximately 650 nm. In addition, we apply a surface passivation layer of 1,3-propane-diammonium iodide and butylammonium iodide ($PDAI_2$ + BAI)[56] to improve the band alignment at the perovskite/C_{60} interface. This dual-molecular passivation layer functions through chemically interacting with surface defect sites to form stable chemical bonds (chemical passivation) and by repelling holes (field-effect passivation), directing them back to the opposite side.[57] As a result, charge carrier management (especially electrons) is further improved, leading to higher V_{OC} and PCE (see Fig. S13–S18, ESI†).

In Fig. 4(B), the $\nu \times f$ parameter is applied to quantitatively demonstrate how a series of optimizations enhance charge carrier management in the PSTSC. In this study, the $\nu \times f$ of the tandem cell increases from 0.58 to 0.7 by annealing the silicon bottom solar cell, further improving to 0.75 through HTL optimization, and ultimately reaching 0.794 of the SQ detailed balance limit for FF $\times$ V_{OC}, benefiting from the surface passivation layer. A series of optimizations improved markedly charge carrier management and reduced the gap to the SQ limit, and a highly efficient PSTSC with a 31% PCE is achieved. Fig. 4(C) shows the *J*–*V* characteristics of the champion device, which exhibits a short-circuit current density (J_{SC}), open-circuit voltage (V_{OC}), and fill factor (FF) of 20.05 mA cm^{-2}, 1.912 V, and 80.9%, respectively. Fig. 4(D) presents the external quantum efficiency (EQE) of the champion device, where the J_{ph} values for the perovskite top cell and silicon bottom cell under AM1.5 illumination is 20.54 mA cm^{-2} and 19.85 mA cm^{-2}, respectively. A J_{ph} mismatch of 0.69 mA cm^{-2} has been observed between the two sub-cells, which can be addressed by adjusting the perovskite layer thickness or the bandgap of perovskite to achieve better current matching. This optimization could further boost

Open Access Article. Published on 06 May 2025. Downloaded on 1/30/2026 3:27:15 AM.
This article is licensed under a Creative Commons Attribution 3.0 Unported Licence.

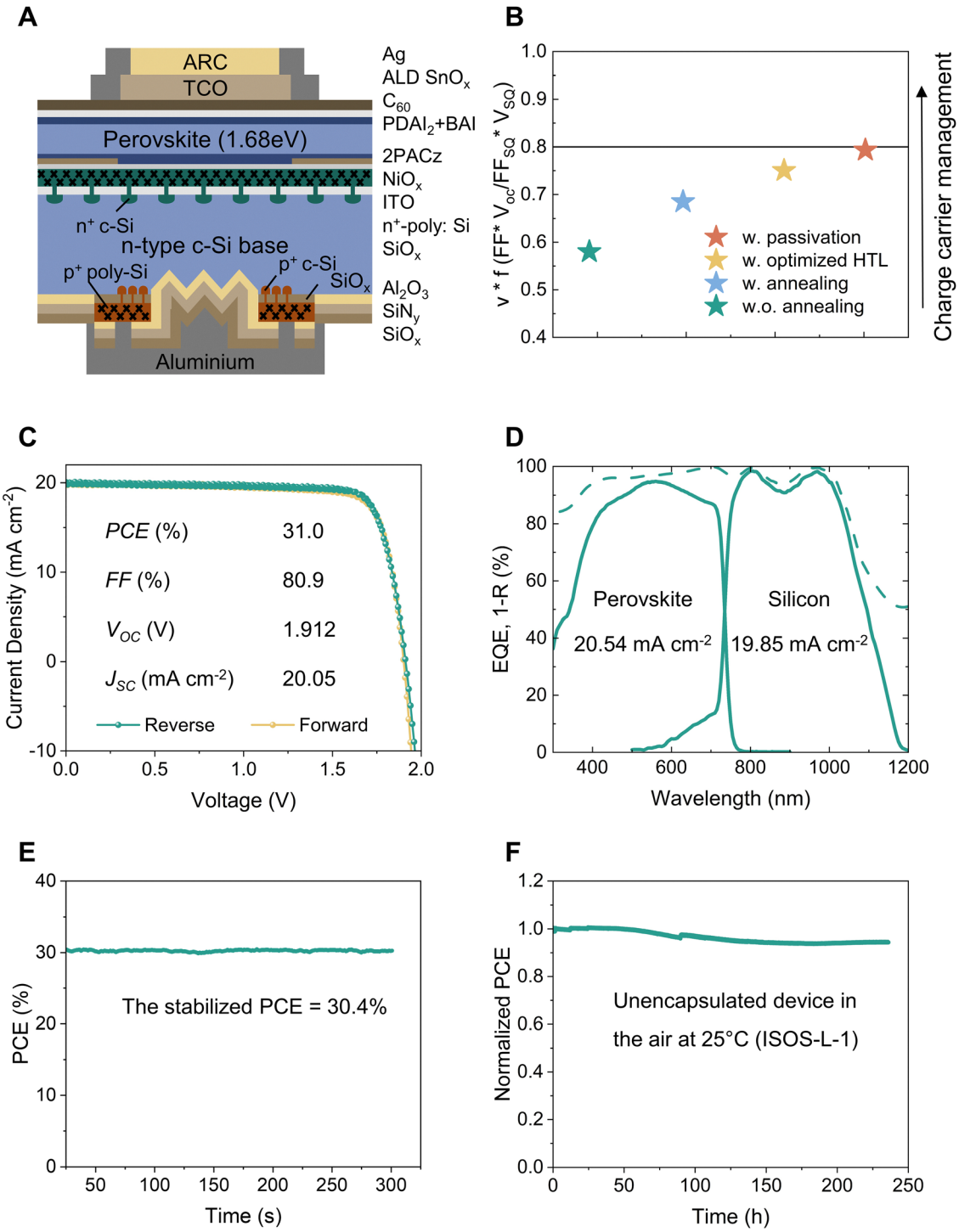

Fig. 4 (A) The schematic illustration of the perovskite–silicon tandem solar cell based on a Si solar cell with POLO junctions. (B) Charge carrier management assessment based on the fraction of Shockley–Queisser limitation for V_{OC} and FF through annealing treatment, optimized HTL, and surface passivation layer. (C) A representative J–V curve for the champion cell. (D) Measured external quantum efficiency (EQE) spectra and reflection (denoted as 1-R) of the perovskite and silicon sub-solar cells, with integrated photocurrent densities of 20.54 mA cm^{-2} (perovskite) and 19.85 mA cm^{-2} (silicon). (E) The 5-minute maximum power point tracking (MPPT) of optimized tandem solar cells. (F) The long-term maximum power point tracking (MPPT) results of the unencapsulated tandem cells under one sun intensity, 25 °C, and 30% relative humidity (ISOS-L-1), retaining 93% of its initial efficiency after 240 hours.

the tandem device's J_{SC} and improve the overall PCE. Fig. 4(E) shows the 5-minute maximum power point tracking (MPPT) measurement, indicating that the tandem cell can operate stably at an efficiency exceeding 30%. Additionally, the long-term stability of the unencapsulated tandem device is evaluated under ISOS-L1 conditions in the ambient environment (25 °C and

 This journal is © The Royal Society of Chemistry 2025

Open Access Article. Published on 06 May 2025. Downloaded on 1/30/2026 3:27:15 AM. This article is licensed under a Creative Commons Attribution 3.0 Unported Licence.

relative humidity of 30%). As shown in Fig. 4(F), after 240 hours of continuous MPPT measurement, the device retains 93% of its initial efficiency. The extrapolated T_{80} lifetime is estimated to be 740 hours.

Conclusion

In this work, we develop the highly efficient 2T-PSTSC based on POLO (equivalent to TOPCon) Si bottom cells. By systematically addressing key challenges in integrating POLO-Si bottom solar cells with perovskite top solar cells, we establish an effective strategy to enhance charge carrier management, reduce recombination losses, and improve device stability. A critical advancement in our approach is the annealing treatment applied to the n-type POLO junction after ITO sputtering and before HTL and perovskite deposition. This process effectively heals sputtering-induced defects, likely further improves Al/p^+ poly-Si contacts, restoring carrier lifetime, and thus enhances FF and V_{OC} of the POLO-Si bottom cell. The silicon bottom cells achieve an iV_{OC} of 730 mV and an iFF of 85.1% at a half-sun illumination assumption, while the passivated p-POLO contacts on localized planar regions of the otherwise textured rear surface optimize light trapping and carrier selectivity. These improvements are validated through infrared lifetime mapping, statistical device performance analysis and the numerical simulation.

Moreover, we investigate the material selection and morphology control on the HTL side of the perovskite top solar cell. We find that the combination of an ultrathin-sputtered NiO_x and SAM leads to a densely distributed micro-island morphology, which facilitates better SAM adhesion and modulates the growth of high-quality perovskite films, enabling effective regulation of charge carrier recombination and transport, thereby improving charge carrier management. This is confirmed by AFM, PLQY, TRPL, light-intensity-dependent iV_{OC} measurements, and PL intensity maps. Finally, we achieve a 31% PSTSC based on POLO-Si, which retains 93% of its initial efficiency after operating for 240 hours at maximum power point under one sun intensity, 25 °C, and 30% relative humidity (ISOS-L-1) without any encapsulation. The projected T_{80} lifetime is approximately 740 hours.

These findings emphasis the distinct material and processing requirements for POLO-based tandem devices, highlighting the need for dedicated research rather than direct extrapolation from single-junction PSCs to PSTSCs. Moving forward, further refinements in passivation strategies, recombination junction engineering, and optical management will be essential to push POLO-Si perovskite tandem solar cells closer to the SQ limit, paving the way for next-generation high-efficiency and industrially scalable photovoltaics.

Author contributions

U. W. Paetzold, R. Guo and X. Liu conceived the idea. U. W. Paetzold, R. Peibst and R. Guo supervised the project and process. U. W. Paetzold, R. Peibst and R. Guo helped with revising the manuscript. X. Liu prepared perovskite films, fabricated single junction and tandem devices, conducted most of the characterizations, X. Liu, M. Rienäcker and R. Peibst wrote the original manuscript. M. Rienäcker fabricated the silicon bottom cell and performed characterization for silicon. M. Gholipoor, L. Fang and F. Sadegh helped with the optimization of tandem cells. B. Hacene performed the TRPL measurement and data analysis. J. Petermann carried out the PL imaging. T. Zhao performed XRD, SEM and EDX measurements. R. Cai assisted in AFM measurements. H. Hu and T. Feeney assisted ALD deposition. R. Guo performed simulations. P. Faßl, and U. Lemmer offered laboratory resources. All authors discussed the results and contributed to the manuscript.

Data availability

The data supporting this article have been included as part of the ESI.† Further information and requests for resources should be directed to and will be fulfilled by the corresponding author.

Conflicts of interest

The authors declare no conflict of interest.

Acknowledgements

The authors thank the whole ''perovskite task force'' at KIT for fruitful discussions and assistance. Financial support by the Helmholtz Association *via* the Solar Technology Acceleration Platform (Solar TAP), the project Zeitenwende (Accelerated transfer of next-generation solar cells into mass production), and the program-oriented funding IV of the Helmholtz Association (Materials and Technologies for the Energy Transition, Topic 1: Photovoltaics and Wind Energy, Code: 38.01.04) is highly acknowledged. This study further receives financial support from the German Federal Ministry for Economic Affairs and Climate Action (BMWK) through the projects 27Plus6 (03EE1056A/B) as well as the program ''zukunft.niedersachsen'' by the Ministry of Science and Culture in Lower Saxony. Furthermore, the authors especially thank Somayeh Moghadamzadeh, Ronja Pappenberger, Ting Pan, Rohit Chavan, Qihao Jin, Julian Petry, Yujing Wang. We thank Guido Glowatzki, Heike Kohlenberg, Sarah Spätlich, Mircea Turcu and Renate Winter for bottom cell processing.

References

1 NREL, Best Research-Cell Efficiency Chart, **https://www.nrel.gov/pv/cell-efficiency.html**.
2 W. Shockley and H. Queisser, *Renewable energy*, Routledge, 2018, pp. Vol2_35–Vol32_54.
3 A. Al-Ashouri, E. Köhnen, B. Li, A. Magomedov, H. Hempel, P. Caprioglio, J. A. Márquez, A. B. Morales Vilches, E. Kasparavicius and J. A. Smith, *Science*, 2020, **370**, 1300–1309.

Open Access Article. Published on 06 May 2025. Downloaded on 1/30/2026 3:27:15 AM. This article is licensed under a Creative Commons Attribution 3.0 Unported Licence.

4 E. Aydin, E. Ugur, B. K. Yildirim, T. G. Allen, P. Dally, A. Razzaq, F. Cao, L. Xu, B. Vishal and A. Yazmaciyan, *Nature*, 2023, **623**, 732–738.
5 Y. Chen, N. Yang, G. Zheng, F. Pei, W. Zhou, Y. Zhang, L. Li, Z. Huang, G. Liu and R. Yin, *Science*, 2024, **385**, 554–560.
6 X. Y. Chin, D. Turkay, J. A. Steele, S. Tabean, S. Eswara, M. Mensi, P. Fiala, C. M. Wolff, A. Paracchino and K. Artuk, *Science*, 2023, **381**, 59–63.
7 H. Li and W. Zhang, *Chem. Rev.*, 2020, **120**, 9835–9950.
8 J. Liu, M. De Bastiani, E. Aydin, G. T. Harrison, Y. Gao, R. R. Pradhan, M. K. Eswaran, M. Mandal, W. Yan and A. Seitkhan, *Science*, 2022, **377**, 302–306.
9 J. Liu, Y. He, L. Ding, H. Zhang, Q. Li, L. Jia, J. Yu, T. W. Lau, M. Li and Y. Qin, *Nature*, 2024, **635**, 596–603.
10 S. Mariotti, E. Köhnen, F. Scheler, K. Sveinbjörnsson, L. Zimmermann, M. Piot, F. Yang, B. Li, J. Warby and A. Musiienko, *Science*, 2023, **381**, 63–69.
11 L. Qiao, T. Ye, T. Wang, W. Kong, R. Sun, L. Zhang, P. Wang, Z. Ge, Y. Peng and X. Zhang, *Adv. Energy Mater.*, 2024, **14**, 2302983.
12 D. Turkay, K. Artuk, X.-Y. Chin, D. Jacobs, S.-J. Moon, A. Walter, M. Mensi, G. Andreatta, N. Blondiaux and H. Lai, *Joule*, 2024, **8**, 1735–1753.
13 E. Ugur, A. A. Said, P. Dally, S. Zhang, C. E. Petoukhoff, D. Rosas-Villalva, S. Zhumagali, B. K. Yildirim, A. Razzaq and S. Sarwade, *Science*, 2024, **385**, 533–538.
14 G. Yang, Z. Ni, Z. J. Yu, B. W. Larson, Z. Yu, B. Chen, A. Alasfour, X. Xiao, J. M. Luther and Z. C. Holman, *Nat. Photonics*, 2022, **16**, 588–594.
15 R. Peibst, U. Römer, Y. Larionova, M. Rienäcker, A. Merkle, N. Folchert, S. Reiter, M. Turcu, B. Min and J. Krügener, *Sol. Energy Mater. Sol. Cells*, 2016, **158**, 60–67.
16 S. Jiang, Z. Ding, X. Li, L. Zhang, Z. Ying, X. Yang, Z. Yang, W. Yang, Y. Zeng and J. Ye, *Adv. Funct. Mater.*, 2024, 2401900.
17 B. Li, M. Härtel, A. Al-Ashouri, M. Simmonds, I. Taupitz, L. Kegelmann, E. Jarzembowski, F. Frühauf, E. Köhnen and L. Korte, *ACS Energy Lett.*, 2024, **9**, 4550–4556.
18 X. Li, Z. Ying, X. Wang, Y. Zeng, X. Yang and J. Ye, *Inf. Funct. Mater.*, 2024, **1**, 160–180.
19 L. Wang, N. Wang, X. Wu, B. Liu, Q. Liu, B. Li, D. Zhang, N. Kalasariya, Y. Zhang and X. Yan, *Adv. Mater.*, 2025, 2416150.
20 J. Zheng, Z. Ying, Z. Yang, Z. Lin, H. Wei, L. Chen, X. Yang, Y. Zeng, X. Li and J. Ye, *Nat. Energy*, 2023, **8**, 1250–1261.
21 X. Guo, Z. Ying, X. Li, M. Zhang, S. Su, J. Zheng, H. Du, Y. Sun, J. Wu and L. Liu, *Adv. Energy Mater.*, 2025, 2403021.
22 Z. Liu, Q. Han, Q. Wu, H. Du, M. Liao, W. Liu, Z. Yang, Y. Zeng and J. Ye, *Mater. Today Energy*, 2024, **46**, 101721.
23 Trinasolar, Trinasolar Announces Efficiency of 26.58% for n-type TOPCon cells, Setting the 28th World Record, **https://static.trinasolar.com/en-apac/resources/newsroom/aptrinasolar-announces-efficiency-2658-n-type-topcon-cells-setting-28th-world**, (accessed 11.21, 2024).
24 N. L. Chang, G. K. Poduval, B. Sang, K. Khoo, M. Woodhouse, F. Qi, M. Dehghanimadvar, W. M. Li, R. J. Egan and B. Hoex, *Prog. Photovoltaics Res. Appl.*, 2023, **31**, 414–428.
25 B. Kafle, B. S. Goraya, S. Mack, F. Feldmann, S. Nold and J. Rentsch, *Sol. Energy Mater. Sol. Cells*, 2021, **227**, 111100.
26 A. Louwen, W. G. van Sark, R. E. Schropp, W. C. Turkenburg and A. P. Faaij, *IEEE 39th Photovoltaic Specialists Conference (PVSC)*, 2013, pp. 3357–3361.
27 J. Zhou, X. Su, Q. Huang, B. Zhang, J. Yang, Y. Zhao and G. Hou, *J. Mater. Chem. A*, 2022, **10**, 20147–20173.
28 L. Wang, Y. Zhang, M. Kim, M. Wright, R. Underwood, R. S. Bonilla and B. Hallam, *Prog. Photovoltaics Res. Appl.*, 2023, **31**, 1442–1454.
29 Y. Larionova, M. Turcu, S. Reiter, R. Brendel, D. Tetzlaff, J. Krügener, T. Wietler, U. Höhne, J. D. Kähler and R. Peibst, *Phys. Status Solidi A*, 2017, **214**, 1700058.
30 R. King, R. Sinton and R. Swanson, *Appl. Phys. Lett.*, 1989, **54**, 1460–1462.
31 M. A. Ruiz-Preciado, F. Gota, P. Fassl, I. M. Hossain, R. Singh, F. Laufer, F. Schackmar, T. Feeney, A. Farag and I. Allegro, *ACS Energy Lett.*, 2022, **7**, 2273–2281.
32 R. Peibst, M. Rienäcker, Y. Larionova, N. Folchert, F. Haase, C. Hollemann, S. Wolter, J. Krügener, P. Bayerl and J. Bayer, *Sol. Energy Mater. Sol. Cells*, 2022, **238**, 111560.
33 S. Mariotti, K. Jäger, M. Diederich, M. S. Härtel, B. Li, K. Sveinbjörnsson, S. Kajari-Schröder, R. Peibst, S. Albrecht and L. Korte, *Solar RRL*, 2022, **6**, 2101066.
34 F. Haase, B. Min, C. Hollemann, J. Krügener, R. Brendel and R. Peibst, *Prog. Photovoltaics Res. Appl.*, 2021, **29**, 516–523.
35 B. Min, N. Wehmeier, T. Brendemuehl, A. Merkle, F. Haase, Y. Larionova, L. David, H. Schulte-Huxel, R. Peibst and R. Brendel, *Solar RRL*, 2020, **4**, 2000435.
36 H. Wu, F. Ye, M. Yang, F. Luo, X. Tang, Q. Tang, H. Qiu, Z. Huang, G. Wang and Z. Sun, *Nature*, 2024, 1–3.
37 R. Brendel, S. Dreissigacker, N.-P. Harder and P. Altermatt, *Appl. Phys. Lett.*, 2008, **93**, 173503.
38 A. Richter, R. Müller, J. Benick, F. Feldmann, B. Steinhauser, C. Reichel, A. Fell, M. Bivour, M. Hermle and S. W. Glunz, *Nat. Energy*, 2021, **6**, 429–438.
39 K. Ramspeck, S. Reißenweber, J. Schmidt, K. Bothe and R. Brendel, *Appl. Phys. Lett.*, 2008, **93**, 102104.
40 F. Haase, C. Hollemann, S. Schäfer, A. Merkle, M. Rienäcker, J. Krügener, R. Brendel and R. Peibst, *Sol. Energy Mater. Sol. Cells*, 2018, **186**, 184–193.
41 Martin A. Green, Ewan D. Dunlop, M. Yoshita, N. Kopidakis, K. Bothe, G. Siefer, X. Hao and Jessica Y. Jiang, *Prog. Photovoltaics Res. Appl.*, 2025, **33**, 3–15.
42 F. Haase, S. Schäfer, C. Klamt, F. Kiefer, J. Krügener, R. Brendel and R. Peibst, *IEEE J. Photovolt.*, 2017, **8**, 23–29.
43 R. Peibst, Y. Larionova, S. Reiter, T. F. Wietler, N. Orlowski, S. Schäfer, B. Min, M. Stratmann, D. Tetzlaff and J. Krügener, *IEEE J. Photovolt.*, 2018, **8**, 719–725.
44 K. Tao, S. Jiang, R. Jia, Y. Zhou, P. Zhang, X. Dai, H. Sun, Z. Jin and X. Liu, *Sol. Energy*, 2018, **176**, 241–247.
45 L. Tutsch, F. Feldmann, J. Polzin, C. Luderer, M. Bivour, A. Moldovan, J. Rentsch and M. Hermle, *Sol. Energy Mater. Sol. Cells*, 2019, **200**, 109960.
46 A. Polman, M. Knight, E. C. Garnett, B. Ehrler and W. C. Sinke, *Science*, 2016, **352**, aad4424.

 This journal is © The Royal Society of Chemistry 2025

Open Access Article. Published on 06 May 2025. Downloaded on 1/30/2026 3:27:15 AM.
This article is licensed under a Creative Commons Attribution 3.0 Unported Licence.

47 O. Er-Raji, C. Messmer, A. J. Bett, O. Fischer, S. K. Reichmuth, F. Schindler, M. Bivour, O. Schultz-Wittmann, J. Borchert and M. Hermle, *Solar RRL*, 2023, **7**, 2300659.
48 M. Bivour, *Silicon heterojunction solar cells: Analysis and basic understanding*, Fraunhofer Verlag, 2017.
49 P. Padhamnath, J. K. Buatis, A. Khanna, N. Nampalli, N. Nandakumar, V. Shanmugam, A. G. Aberle and S. Duttagupta, *Sol. Energy*, 2020, **202**, 73–79.
50 J. Isenberg, S. Riepe, S. W. Glunz and W. Warta, *J. Appl. Phys.*, 2003, **93**, 4268–4275.
51 N. M. Ahmed, F. A. Sabah, H. Abdulgafour, A. Alsadig, A. Sulieman and M. Alkhoaryef, *Results Phys.*, 2019, **13** 102159.
52 Y. Jiang, T. Feurer, R. Carron, G. T. Sevilla, T. Moser, S. Pisoni, R. Erni, M. D. Rossell, M. Ochoa and R. Hertwig, *ACS Nano*, 2020, **14**, 7502–7512.
53 Z. W. Gao, Y. Wang and W. C. Choy, *Adv. Energy Mater.*, 2022, **12**, 2104030.
54 X. He, H. Chen, J. Yang, T. Wang, X. Pu, G. Feng, S. Jia, Y. Bai, Z. Zhou and Q. Cao, *Angew. Chem.*, 2024, **136**, e202412601.
55 T. Kamins, *Polycrystalline silicon for integrated circuits and displays*, Springer Science & Business Media, 2012.
56 H. Chen, A. Maxwell, C. Li, S. Teale, B. Chen, T. Zhu, E. Ugur, G. Harrison, L. Grater and J. Wang, *Nature*, 2023, **613**, 676–681.
57 C. Liu, Y. Yang, H. Chen, J. Xu, A. Liu, A. S. Bati, H. Zhu, L. Grater, S. S. Hadke and C. Huang, *Science*, 2023, **382**, 810–815.